Department of Precision and Microsystems Engineering

MEMS Mechanism for Fine-tuning Geometric Anti-Spring Compression

Name

Report no	:	2024.019
Coach	:	Dr. D. (Davood) Farhadi
Professor	:	Prof. dr. M.K. (Murali) Ghatkesar
Specialisation	:	MSD
Type of report	:	Thesis report
Date	:	9 April 2024

TU Delft Delft University of Technology

Challenge the future

MEMS Mechanism for Fine-tuning Geometric Anti-Spring Compression

A.D. Wassenaar
to obtain the degree of Master of Science at the Delft University of Technology,
to be defended publicly on 23-04-2024 at 15:00
Thesis committee members:
Prof. dr. M.K. (Murali) Ghatkesar (Delft University of Technology, chair),
Dr. D. (Davood) Farhadi (Delft University of Technology, supervisor),
Dr. M.G. (Mark) Beker (Innoseis Sensor Technologies, supervisor)

***Abstract*—The use of geometric anti-springs (GASs) in MEMS accelerometers can not only boost the sensitivity through the static balancing effect, it also introduces the capability to tune the stiffness post-manufacturing by adjusting the balancing force. This paper addresses the challenge of mechanically fine-tuning the stiffness to create the potential for compensating thermal drift of bias (TDB), whereas previous methods focused on doing so electrostatically. Due to the large effect of TDB on integration errors, creating this new method for compensation could help open up the way to more accurate inertial navigation by high-precision MEMS. As the basis of our research we used an existing accelerometer from Innoseis Sensor Technologies (version G6). Based on a theoretical analysis of the TDB, requirements were formulated and a design was developed through a combination of pseudo-rigid body and finite element modelling. By building a macro-scale prototype, we were able to validate our models. It can therefore be concluded that our design provides 8 additional compression steps ranging between 50 and 54 nm based on the model predictions. This proof-of-concept demonstrates to be a new tool in the design of future accelerometers with GASs.**

***Index Terms*—thermal drift of bias (TDB), geometric anti-springs (GASs), MEMS**

I. INTRODUCTION

There are many technologies that play important roles in our society and yet are mostly invisible to the public eye. One of these technologies are high-precision MEMS (micro-electromechanical system) sensors, with applications ranging from seismic sensing to inertial navigation [1]. An example of such a system is the capacitive MEMS accelerometer developed by Boom et al. [2] that makes use of compressed curved leaf springs called geometric anti-spring (GAS) technology to achieve high levels of stiffness reduction. In their design the compression is performed by an anti-reverse ratchet-pawl mechanism that is actuated by an electro-thermal actuator (ETA). Other examples of devices with curved springs include the MEMS gravimeter by Middlemiss et al. [3] and the MEMS sensor by El Mansouri et al. [4], however the springs in these devices are not compressed through a mechanism but move into a compressed position with the help of gravity. One of the possible applications for high-precision MEMS is in inertial navigation systems (INS) [5], however it has been shown by Dai et al. [6] that fabrication errors can cause thermal drift of bias (TDB), and this could lead to a build-up of error over time. According to them, one of the causes is the stiffness asymmetry due to differences in beam width of the springs from these fabrication errors. This idea was also proposed by He et al. [7], who then designed a compensation structure that could passively lower the TDB by centering the anchors in the sensing direction. An advantage for MEMS with GASs is that the stiffness is created through the static-balancing effect. One can therefore change the pre-load to adjust the stiffness. Zhang and Wei [8] already demonstrated a reduced thermal drift of scale-factor (TDSF) by actively compensating the stiffness of their GASs through the application of a DC bias voltage. One could attempt the same strategy to instead reduce the TDB, although in each case the electrostatic compensation could come at the cost of measurement range in closed-loop systems. This is because the bias voltage would probably need to be provided by the feedback electronics, leaving less voltage range for the feedback signal. A compensation method where the stiffness is mechanically adjusted might offer a novel approach to address this issue.

The goal of this work is therefore to design a MEMS mechanism that can fine-tune the compression distance of the GASs in the Innoseis G6 accelerometer, to potentially compensate for TDB as a result of manufacturing tolerances. In order to accomplish this, first, in Section III, the TDB is modelled to find an effective way of compensating the TDB by means of mechanically changing the compression distance of the GASs in the accelerometer. Based on this, requirements are formulated and a mechanism, including an actuator, is designed using different models in Section IV. The paper then describes our method of experimentally validating these models by building a macro-scale prototype in Section V. Last, the results are presented and discussed in Sections VI and VII.

II. BACKGROUND

A. MEMS overview

In Figure 1(a) a Scanning Electron Micriscope (SEM) image of an earlier but similar version of the G6 MEMS accelerometer is displayed. The proof-mass is suspended by sets of GAS in each corner that are shown in close-up in inset (e). The compression stage that compresses each set of GASs can be seen in inset (d), with part of the electrothermal actuator (ETA) that is used for this visible on the right. Since the device is operated in closed-loop, variable-area driving combs are used to provide the feedback force (inset (c)). The displacement of the proof-mass is measured through variable-gap sensing combs, visible in inset (b).

B. Compression stage

To force the GASs to remain into their compressed state without requiring a continuous energy supply during operation, a compression stage is used, schematically depicted in Figure 2. When the ETA pushes against the shuttle, the shuttle springs, consisting of two pairs of three leaf springs, guide it forward until the shuttle pawls hook behind a pair of ratchet teeth. At this point, the ETA can be disengaged while the shuttle remains to rest on the pawls, thus keeping the GASs compressed.

III. MODELLING THE THERMAL DRIFT OF BIAS

In order to model the TDB of the Innoseis MEMS accelerometer version G6 as a function of etch-offsets (i.e. feature width variations from local under- and over-etching), a numerical as well as a Finite Element (FE) model was made. Both models were based on the work of He [7] et al. where static equilibrium along the sensing axis was used to derive the TDB. Since our accelerometer is operated in closed-loop this meant that the TDB would express itself as the thermal drift of the restoring feedback force. Only in-plane effects were considered and bilateral symmetry was assumed around the sensing y-axis. Temperature effects that were included were thermal expansion of the floating structures with the coefficient of thermal expansion (CTE) of silicon, thermal expansion of the anchors, and the temperature dependence of the Young's modulus. This section will elaborate on both models and give a brief discussion on their results.

A. Numerical TDB model

The basis of the numerical model for calculating the TDB was the anti-spring model by Boom [9] (see Section 1.1 in the Supplementary material (SM)) based on the Euler-Bernoulli beam theory. In Figure 3 the relevant dimensions for the model are shown with the displacements due to thermal expansion indicated with the open red arrows. The floating structures are colored in blue and the parts that are fixed to the substrate are marked purple. Similar to the work of Zhang et al. [8] static equilibrium along the y-axis was first applied. However, since our accelerometer is operated in closed-loop the centre of mass was assumed to remain at y=0. Also, thermal expansion changing the compression distance of the GASs was taken into account, in contrast to [8]. Then, considering the displacement of the end points of the springs, this yielded Equation 1.

In this equation, F_{R} is the restoring force provided by the feedback driving combs, H_{C} is the distance between the anchor points of the top and bottom shuttle springs, H_{D} is the distance between the shuttle spring anchor and the centre of the connection point of the GASs to the shuttle, H_{A} is the distance between the centres of the connection points of the top and bottom GASs, y_{p} is the parasitic displacement of the shuttle along the y-axis due to the shortening effect of the shuttle springs, and $K_{\mathrm{y,t}}$ and $K_{\mathrm{y,t}}$ are the stiffnesses of the top and bottom GASs combined respectively. The coefficient α_{eq} represents an equivalent CTE with which the anchor points expand since they are connected to the substrate and will therefore expand in different amount. Due to the static balancing effect of the GASs, the spring stiffness is not only a function of shape parameters (such as length L, width w and height t) and the Young's modulus, but also of compression distance Δx. For this reason each GAS stiffness was modelled as follows:

$$K_y = K_y(\Delta x(\Delta T, \Delta x_i),\ w(\Delta T, \Delta s),\ t(\Delta T),\ L(\Delta T), E(\Delta T)), \tag{2}$$

where Δx_i is the initial compression distance of the GASs, which was later varied for the top springs to investigate its influence on the TDB. Parameter Δs is the etch-offset from the manufacturing process, which was also varied for the top springs, therefore keeping the bottom springs at their nominal width and compression. The temperature difference is indicated by ΔT. The temperature dependence of the Young's modulus for the isotropic material model for silicon was obtained from the work of Bourgeois et al. [10]. They determined a temperature coefficient of about -64 ppm/K for the uniaxial load case at room temperature (25 °C) and this value was adopted for the temperature coefficient of the Young's modulus in this work. The Young's modulus at room temperature was adopted from [9], who calculated the average value along the curve of the GAS to be 156 GPa. A list of all the parameters and dimensions can be found in Table I.

TABLE I: A list of all parameters and dimensions that were used in the simulations of the TDB.

Parameter	Symbol	Value
Length	W_{A}	[CONFIDENTIAL]
	W_{B}	[CONFIDENTIAL]
	W_{C}	[CONFIDENTIAL]
	H_{A}	[CONFIDENTIAL]
	H_{C}	[CONFIDENTIAL]
	H_{D}	[CONFIDENTIAL]
Nominal spring width of the GASs	w	[CONFIDENTIAL]
Initial compression distance of the GASs	Δx_{i}	[CONFIDENTIAL]
Parasitic motion of the shuttle	y_{p}	[CONFIDENTIAL]
Length of the shuttle springs	L_{s}	[CONFIDENTIAL]
Width of the shuttle springs	w_{s}	[CONFIDENTIAL]
Separation distance of the GASs in each corner	-	[CONFIDENTIAL]
Device layer height (out-of-plane)	t	[CONFIDENTIAL]
Isotropic Young's modulus	$E_{\mathrm{isotropic}}$	156 GPa

$$F_{\mathrm{R}} + K_{\mathrm{y,t}}((1+\alpha_{\mathrm{eq}}\Delta T)H_{\mathrm{C}}/2 - (1+\alpha_{\mathrm{Si}}\Delta T)H_{\mathrm{D}} - (1+\alpha_{\mathrm{Si}}\Delta T)H_{\mathrm{A}}/2 + y_{\mathrm{p}}) - K_{\mathrm{y,b}}((1+\alpha_{\mathrm{eq}}\Delta T)H_{\mathrm{C}}/2 - (1+\alpha_{\mathrm{Si}}\Delta T)H_{\mathrm{D}} - (1+\alpha_{\mathrm{Si}}\Delta T)H_{\mathrm{A}}/2 + y_{\mathrm{p}}) = 0. \tag{1}$$

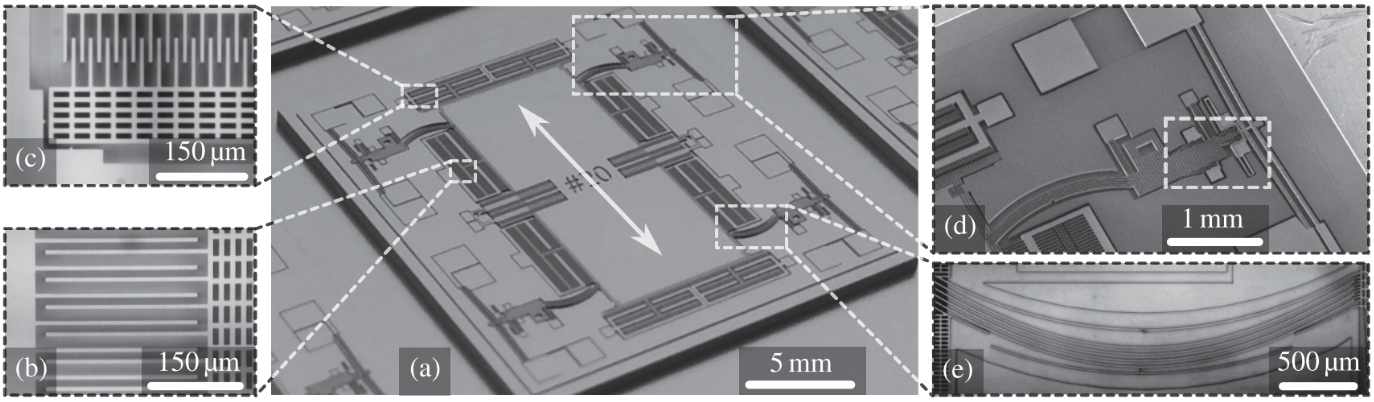

Fig. 1: A scanning electron image of an earlier version of the accelerometer with GASs, from [2]. The double-headed white arrow indicates the y-axis sensing direction.

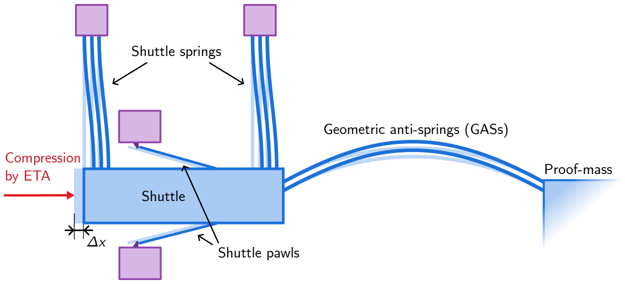

Fig. 2: A schematic illustration of the compression stage that connects to the GASs and the proof-mass. The undeformed initial state is marked in light blue and the anchor points are marked purple.

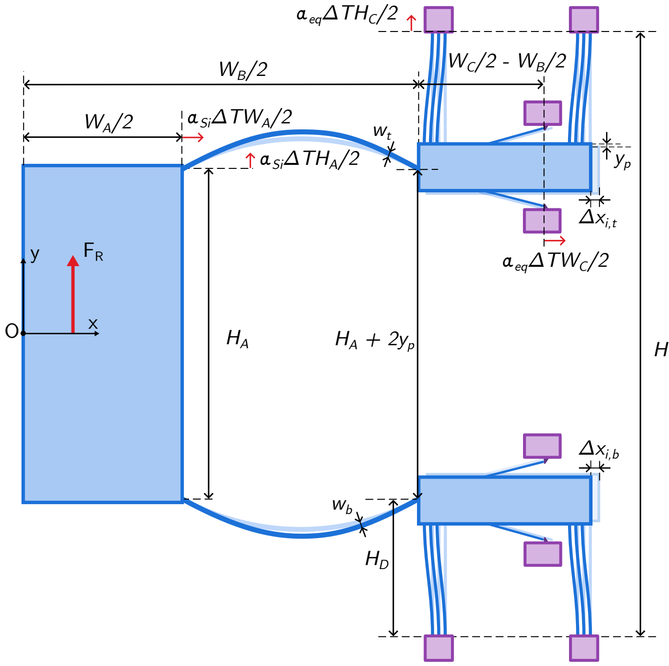

Fig. 3: A schematic illustration of one half of the G6 accelerometer indicating the relevant dimensions and displacements used in the numerical TDB model. For clarity only one GAS is shown per corner instead of two.

B. Finite Element TDB model

To verify the results from the numerical model, a FE model was made using ANSYS Mechanical R2022 for which the CAD file was made using SolidWorks 2022. An overview of the boundary conditions that were applied can be seen in Figure 4. Boundary condition A resembles the restoring force keeping the proof-mass in the centre and the yellow arrows indicate the displacements from the thermal expansion of the anchor-points with coefficient α_{eq}. Bilateral symmetry was applied around the y-axis using the Frictionless support boundary condition on the left edge of the proof-mass (I) to exclude effects from a rotation of the proof-mass. To capture the orientation dependent nature of the material properties of the cubic silicon lattice, we used an orthotropic material model with the values listed in Table II, adopted from [11]. The model was rotated 45 degrees in counter clockwise direction to align the global x-axis with the [110] direction, as is customary in a standard (100) silicon wafer. The temperature dependence of the elastic constants was captured using the linear coefficients for the stiffness matrix elements from [12, Tab. IV] for a boron-doping level of $4.1{\cdot}10^{18}\ \mathrm{cm}^{-3}$: -63 ppm/K for stiffness coefficient c_{11} , -78 ppm/K for stiffness coefficient c_{12} and -48 ppm/K for stiffness coefficient c_{44}.

We used the Static structural module with analysis type set to 2D plane-stress. The motivation for this is provided in the Supplementary material Section 1.3, where several different

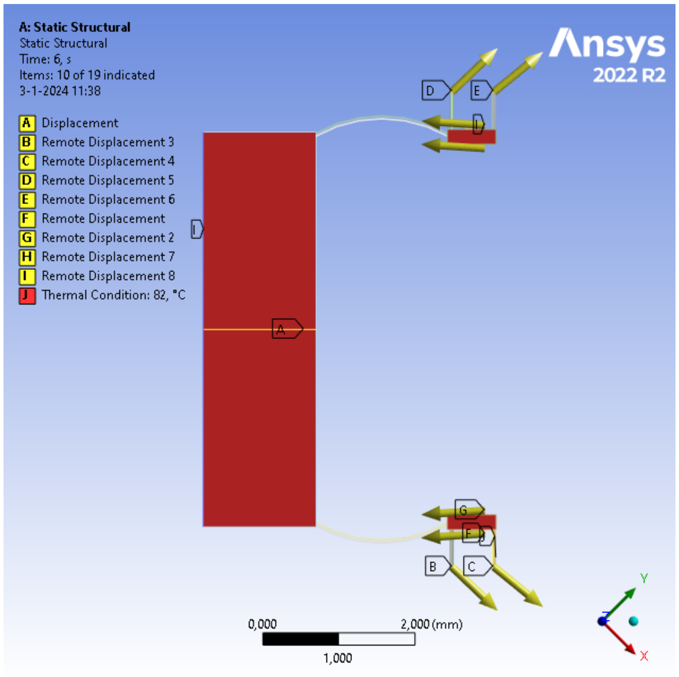

Fig. 4: A screenshot of the FE TDB model in ANSYS Mechanical R2022 with the thermal expansions boundary conditions indicated by the yellow arrows.

FE analyses, both 2D and 3D, were performed on a single GAS using either an isotropic or orthotropic material model. The mesh type was set to quadrilateral with a quadratic element order (2D 8-node structural solid, element type PLANE183) and geometric non-linearity was enabled. A mesh convergence study on the restoring force F_R was first executed that can be found in the Supplementary material Section 3.1. Limited by the computational power available, the proximity gap factor (i.e. the number of elements across each beam) was chosen to be 25 with a mesh growth rate of 1.05 and global mesh size of 10 μm, thus requiring approximately 1.1M elements in all simulations. Then, similar to the numerical model, the etch-offset was varied for the top half of the accelerometer, although now both the width of shuttle pawls and shuttle springs were also taken into account.

TABLE II: Orthotropic material properties of a standard silicon (100) wafer with the axes of the frame of reference [100], [010] and [001], from Hopcroft et al. [11].

Elastic property	Value
E_x, E_y, E_z	165.7 GPa
ν_{yz}, ν_{zx}, ν_{xy}	0.28
G_{yz}, G_{zx}, G_{xy}	79.6 GPa

Fig. 5: A schematic illustration of the cross-section of the G6 accelerometer package showing the different layers that are bonded together (not to scale and thin metal layers not considered).

C. Estimating the equivalent coefficient of thermal expansion

Now that both models were ready, a value for the coefficient α_{eq}, that describes the thermal expansion of the anchors, had to be obtained, which will be referred to as the equivalent CTE. The layered 'sandwich' structure of the cross-section of the G6 accelerometer chip gives rise to this equivalent CTE that describes the displacement of the anchors of the GASs. These different layers are illustrated in Figure 5 and the values of the coefficients of thermal expansion for the individual layers are listed in Table III. The metal bonding layers were not considered because their combined thickness was less than 1 μm, and for this reason we expected them to have little effect. Due to the uncertainty in the thickness of the adhesive layer, the equivalent coefficient of thermal expansion α_{eq} could not be precisely determined. Therefore it was estimated to be the average between α_{Si} and $\alpha_{\text{Al}-440}$. The instantaneous coefficient of thermal expansion was determined by Okada and Tokumaru [13] to be:

$$\alpha_{\text{Si,inst}} = \\ 3.725 \cdot 10^{-6}(1 - e^{-5.88 \cdot 10^{-3}(T-124)}) + 5.548 \cdot 10^{-10}\ T. \tag{3}$$

The (secant) coefficient of thermal expansion was then obtained using:

$$\alpha_{\text{Si}} = \frac{\int_{T_0}^{T} \alpha_{\text{Si,inst}}(T)\ dT}{T - T_0}, \tag{4}$$

where T_0 is the reference temperature, in our case 20 °C. For the equivalent CTE this yielded:

$$\alpha_{\text{eq}} = \frac{\int_{T_0}^{T} \left(\frac{\alpha_{\text{Si,inst}}(T) + \alpha_{\text{Al}-440}}{2}\right) dT}{T - T_0}. \tag{5}$$

D. Etch-offset quantification

Using measurement data of the variations of the read-out comb capacitance, we estimated the die-to-die variation in the etch-offset to be at most around 0.2 μm (see the Supplementary material Section 2). As each set of GASs is

TABLE III: Thermal properties of the G6 accelerometer package assembly.

Material	Symbol	Value (ppm/K)	Layer thickness (μm)
Silicon	α_{Si}	$\alpha_{\text{Si}}(\Delta T)$	device: [CONFIDENTIAL], handle: 400
Silicon dioxide	α_{SiO2}	0.55	top: 5, bottom 4
Alumina (Kyocera A-440)	$\alpha_{\text{Al}-440}$	7.1	1000
Adhesive (Ablestik 84)	$\alpha_{\text{Ab}-84}$	40	~25

located in a corner of the die, we used this value as the maximum variation in thickness between the top and bottom springs, including the beams in their compression stage for the FE model.

E. TDB model results

Using both models, the restoring force could now be calculated as a function of the the spring width difference between the top and bottom half of the accelerometer, keeping the bottom half at its nominal dimensions. Seeing that the mesh convergence stalled at around 10 nN (See Supplementary material Section 3.1) because of the limited computational power, the etch-offset was magnified by a factor 10 (2 μm) to reduce the influence of this convergence error. Plotting the restoring force F_R as a function of the spring width difference $(w_\mathrm{t} - w_\mathrm{b})$ revealed a minimum in its temperature dependence for applied temperature differences ΔT ranging from -20 K to 60 K relative to room temperature (20°C). For identical compression distances between the top and bottom springs this minimum appeared at a spring width difference of zero. However, by changing the compression distance of the top springs this minimum would shift. This is shown in Figure 6 for an extra compression of the top springs of 0.8 μm where the minimum appeared at a spring width difference of 0.48 μm. Five additional plots showing different compression distances can be found in the Supplementary material Section 3.1.

To verify this phenomenon, the same TDB simulations were performed using the FE model, for which the results can be viewed in the Supplementary material Section 3.2. In Figure 7 the data points corresponding to the minima of the TDB from both models are shown. The error bars in the FE model data were estimated based on the limited amount of data points to precisely locate the minima of the TDB. The most important observation here was that the minima in the TDB followed the same trend as the numerical model, thereby verifying its behaviour. This plot now served as the basis of the requirements for the mechanism that was subsequently designed and will be discussed next.

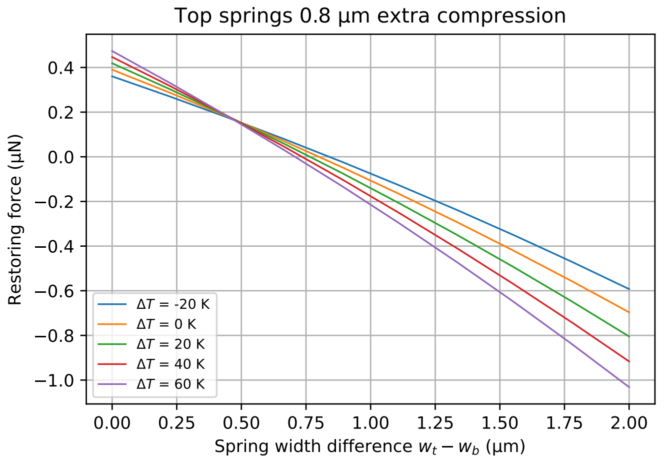

Fig. 6: The restoring force as a function of the spring width difference for different temperatures, where the GASs in the top half of the accelerometer are compressed an additional 0.8 μm

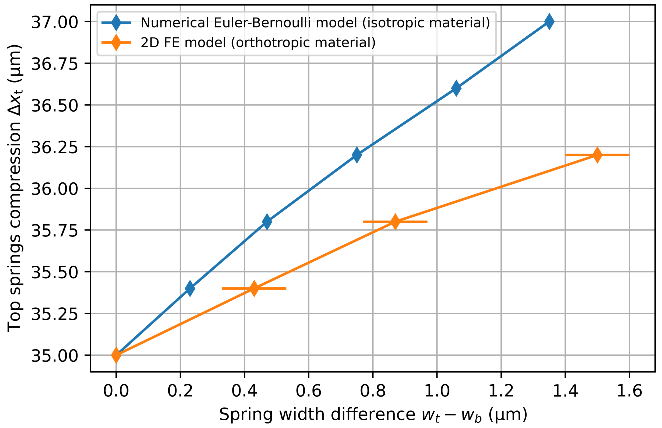

Fig. 7: A plot showing the outcome of the numerical and FE TDB model where for each spring width difference a minimum was identified. The error bars indicate the uncertainty in the location of the TDB minima because of the small amount of data points.

IV. DESIGN METHODOLOGY

A. Functional requirements and constraints

Based on the outcome of the analysis of the minima of the TDB, the functional requirements that the mechanism should satisfy were formulated. These can be found in Table IV. The fist requirement (R1) was formulated to facilitate the movement of the shuttle on top of the initial 35 μm and its specification followed from the plot in Figure 7. Here, for a spring width difference of 0.2 μm, the numerical model dictated an extra compression of approximately 400 nm and this value was chosen to serve as a worst case. The second requirement was added simply to encompass the ability to change the compression distance of the GASs by providing enough force. The corresponding specification was separately defined for compression and decompression as decompression would have an entirely different operating principle compared to simply compressing the shuttle beyond the initial 35 μm. Requirement number 3 prescribes that the compression distance should be maintained passively to eliminate energy consumption during operation. The last requirement (R4) was formulated not as an independent requirement but as being dependent on R3 in the case of using a ratchet and pawl to achieve discrete compression steps of the shuttle. For in that case, being limited by the minimum feature size (see constraint C2) that prescribes a ratchet tooth pitch of minimal ∼10 μm, the motion attenuation factor between the pawl and the shuttle should be (10 μm/50 nm =) 200 when using a single pawl. This factor can be decreased by using multiple pawls next to each other shifted by 10 μm/n, where n is the number of pawls, as will be discussed in Section IV-C2.

Next, the constraints were formulated that the mechanism should comply with, listed as C1 to C7 in Table IV. For constraint C5 the fracture strength was obtained from the work of DelRio et al. [14], who reviewed a large number of sources to provide a comprehensive overview on the fracture strength in MEMS. Here, a fracture strength between 0.5 to 5 GPa was reported for the micro-scale region and we picked the average between these values (2.7 GPa) with safety factor of 3 (900 MPa) to be the maximum allowable principal stress in our design.For the calculation of the critical buckling load for constraint C6 in the flexures, Euler's buckling formula was used:

$$F_{\text{buckle}} = \frac{\pi^2 E I_{\text{z}}}{L^2}, \tag{6}$$

where E is the Young's modulus, I_{z} is the second moment of area around the out-of-plane z-axis and L is the length of the beam.

B. Preliminary design

Based on the functional requirements and constraints, multiple concepts were generated. Then, using a method of weighted criteria, the most promising concept was selected (see the Supplementary material Sections 4.1-4.4). In Figure 8 this concept is schematically depicted. For clarity, rigid elements are marked blue, flexible elements are marked orange, anchor points that are fixed to the substrate are marked purple and the V-beam ETA with its anchor points are marked red. The grey-marked element indicates the anchor that contains the ratchet that will allow the mechanism to stay fixed in a discrete range of positions without requiring continuous energy supply. The amplification stage and the actuator stage were physically separated by a gap of 3.4 μm to prevent the emergence of a parasitic capacitance from the electrical circuit of the ETA, as prescribed by constraint C4. By sending a current through the anchor points of the ETA, the actuator pushes with a lever with displacement u_{ETA} against the amplification stage with displacement u_1. The pawl with end-point Z, which will be referred to as the attenuation stage pawl, then moves relative to the ratchet with displacement u_{z} and at the same time joint H moves with displacement u_2 around joint I. The instant centre IC will cause this motion to be converted to downward displacement of joint E with u_3, being guided by the parallel leaf flexures with length L_1. Lastly, since the shuttle pawl is being pushed downwards with displacement u_3 at point U, the shuttle will displace with displacement u_{out}. Throughout this report, point U, that represents the contact point of the shuttle pawl, was modelled as a revolute joint. To avoid non-linearity to appear in the input-output relationship u_{ETA} and u_{out}, it was decided to distribute the attenuation ratios of the attenuation stage in approximate equal amounts: 4x for u_{z}/u_2, 5x for u_2/u_3 and 5x for u_3/u_{out}. Here it was assumed that u_2 would be approximately equal to $u_{2'}$.

C. Dimensioning, phase 1

The dimensioning of all the links and flexures including the ETA was done in two phases. Phase 1 consisted of obtaining coarse dimensions using pseudo-rigid-body (PRB) modelling to make the design fit on the footprint. Then in Phase 2, the dimensions were fine-tuned with the aid of finite element (FE) modelling to comply with the constraints and to serve as a verification for the PRB model.

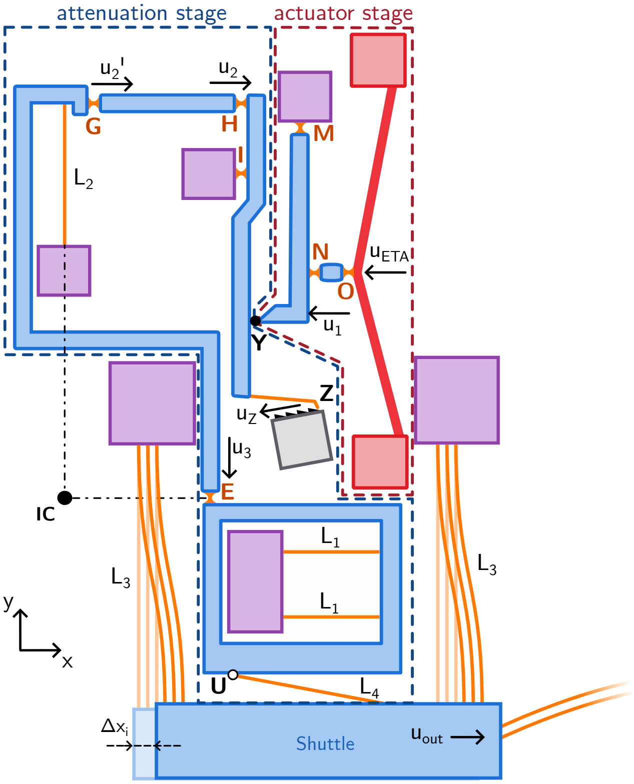

Fig. 8: A schematic illustration of the preliminary design. The blue parts represent floating structures, the purple parts represent the fixed anchors and the orange parts indicate the flexures. The ETA that actuates the whole mechanism is colored in red.

1) Pseudo-Rigid-Body model: After the preliminary design was completed, a PRB model was made based on the work of Howell et al. [15] to model the forces and displacements. A schematic overview of the PRBM can be found in Figure 10. Work on the PRBM was started by first converting all small-length flexural pivots (E,G,H,I,M,N,O) to rotational joints with torsional springs located at the centre of the flexures. Each having stiffness:

$$K = \frac{E I_{\text{z}}}{L}, \tag{7}$$

where E is the Young's modulus, I_{z} is the second moment of area around the z-axis and L is the length of the flexure. Then the leaf springs with lengths L_1, L_2 and L_3 were converted to their rigid-body equivalent with a characteristic radius factor γ of 0.85. Here, for each torsional spring we used stiffness [16]:

$$K = \gamma K_{\theta} \frac{E I_z}{L}, \tag{8}$$

TABLE IV: An overview of all requirements and constraints

Requirement	Specification
R1. Provide a linear range of motion to the shuttle	400±40 nm
R2. Compress or decompress the GAS pairs plus the shuttle springs	For compression: ≥22.5mN, for decompression: *unknown* mN
R3. Provide an adjustable extra compression distance of the GAS pairs without requiring a continuous energy supply	Continuous compression distance: [-] , discrete compression distance: 8 steps of 50±5 nm
R4. Provide linear motion attenuation between the ratchet and the shuttle output displacement steps*	Attenuation factor in each step: 200/n ±10% where n is the number of ratchet-pawl pairs.

Constraint	Specification
C1. The mechanism must fit on the Innoseis accelerometer version G6	See the footprint image in Figure 9
C2. The mechanism must be able to be manufactured using the current Innoseis manufacturing process	Minimal beam width: [CONFIDENTIAL] Minimal pattern spacing: [CONFIDENTIAL] Minimal feature size: [CONFIDENTIAL] Device layer height: [CONFIDENTIAL]
C3. The mechanism should be operable in a high-vacuum	[CONFIDENTIAL]
C4. The mechanism should not impair the operation of the accelerometer	
C5. The maximum principal tensile stress in the mechanism may not exceed a certain value	900 MPa
C6. In slender beams, the longitudinal force must be removed a certain factor from the critical buckling load	Factor of safety: 3
C7. The (out-of-plane) sag at any point must not be more than a certain value	5 μm

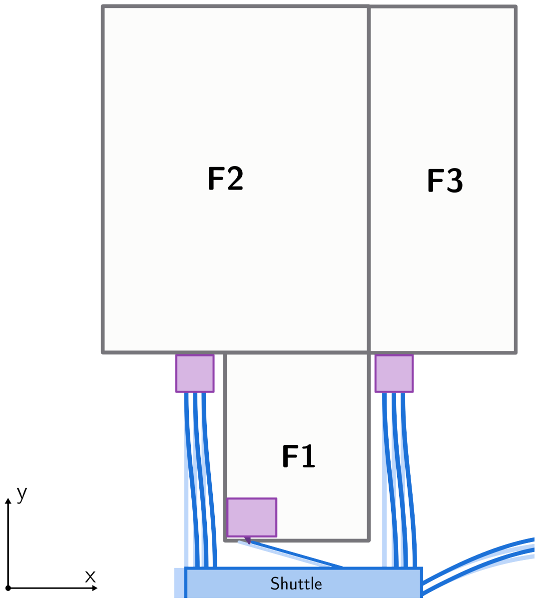

Fig. 9: The available footprint on the G6 accelerometer, split into three section F1 to F3.

where K_θ is the stiffness coefficient and was set to 2.65. In the whole PRB model 169 GPa was used for the Young's modulus since most flexures aligned with the x- or y-axis. The loop-closure equations could then be written down for the five loops O'ONMO', IYMI, JFGHIJ, CDEFJC and PQTUDCP, where O' indicates the initial position of O [17]. This yielded:

$$\mathbf{r}_{\mathrm{O'/O}} + \mathbf{r}_{\mathrm{O/N}} + \mathbf{r}_{\mathrm{N/M}} + \mathbf{r}_{\mathrm{M/O'}} = 0, \tag{9}$$

$$\mathbf{r}_{\mathrm{I/Y}} + \mathbf{r}_{\mathrm{Y/M}} + \mathbf{r}_{\mathrm{M/I}} = 0, \tag{10}$$

$$\mathbf{r}_{\mathrm{J/F}} + \mathbf{r}_{\mathrm{F/G}} + \mathbf{r}_{\mathrm{G/H}} + \mathbf{r}_{\mathrm{H/I}} + \mathbf{r}_{\mathrm{I/J}} = 0, \tag{11}$$

$$\mathbf{r}_{\mathrm{C/D}} + \mathbf{r}_{\mathrm{D/E}} + \mathbf{r}_{\mathrm{E/F}} + \mathbf{r}_{\mathrm{F/J}} + \mathbf{r}_{\mathrm{J/C}} = 0, \tag{12}$$

$$\mathbf{r}_{\mathrm{P/Q}} + \mathbf{r}_{\mathrm{Q/T}} + \mathbf{r}_{\mathrm{T/U}} + \mathbf{r}_{\mathrm{U/D}} + \mathbf{r}_{\mathrm{D/C}} + \mathbf{r}_{\mathrm{C/P}} = 0. \tag{13}$$

In our vector notation, $\mathbf{r}_{\mathrm{A/B}}$ refers to a vector pointing from point A to point B. Each vector was then expressed in its polar complex form, resulting in:

$$\begin{split} L_{\mathrm{O'/O}} \mathrm{e}^{0j} + L_{\mathrm{O/N}} \mathrm{e}^{\theta_{\mathrm{O/N}} j} + \\ L_{\mathrm{N/M}} \mathrm{e}^{\theta_{\mathrm{N/M}} j} + L_{\mathrm{M/O'}} \mathrm{e}^{\theta_{\mathrm{M/O'}} j} = 0, \end{split} \tag{14}$$

$$L_{\mathrm{I/Y}} \mathrm{e}^{\theta_{\mathrm{I/Y}} j} + L_{\mathrm{Y/M}} \mathrm{e}^{\theta_{\mathrm{Y/M}} j} + L_{\mathrm{M/I}} \mathrm{e}^{\theta_{\mathrm{M/I}} j} = 0, \tag{15}$$

$$\begin{split} L_{\mathrm{J/F}} \mathrm{e}^{\theta_{\mathrm{J/F}} j} + L_{\mathrm{F/G}} \mathrm{e}^{\theta_{\mathrm{F/G}} j} + L_{\mathrm{G/H}} \mathrm{e}^{\theta_{\mathrm{G/H}} j} + \\ L_{\mathrm{H/I}} \mathrm{e}^{\theta_{\mathrm{H/I}} j} + L_{\mathrm{I/J}} \mathrm{e}^{\theta_{\mathrm{I/J}} j} = 0, \end{split} \tag{16}$$

$$\begin{split} L_{\mathrm{C/D}} \mathrm{e}^{\theta_{\mathrm{C/D}} j} + L_{\mathrm{D/E}} \mathrm{e}^{\theta_{\mathrm{D/E}} j} + L_{\mathrm{E/F}} \mathrm{e}^{\theta_{\mathrm{E/F}} j} + \\ L_{\mathrm{F/J}} \mathrm{e}^{\theta_{\mathrm{F/J}} j} + L_{\mathrm{J/C}} \mathrm{e}^{\theta_{\mathrm{J/C}} j} = 0, \end{split} \tag{17}$$

$$\begin{split} L_{\mathrm{P/Q}} \mathrm{e}^{\theta_{\mathrm{P/Q}} j} + L_{\mathrm{Q/T}} \mathrm{e}^{\theta_{\mathrm{Q/T}} j} + L_{\mathrm{T/U}} \mathrm{e}^{\theta_{\mathrm{T/U}} j} + \\ L_{\mathrm{U/D}} \mathrm{e}^{\theta_{\mathrm{U/D}} j} + L_{\mathrm{D/C}} \mathrm{e}^{\theta_{\mathrm{D/C}} j} + L_{\mathrm{C/P}} \mathrm{e}^{\theta_{\mathrm{C/P}} j} = 0. \end{split} \tag{18}$$

Last, to solve each vector equation, the vectors were split up into their real and imaginary parts and solved simultaneously for 2 selected unknowns:

$$\sum_{i=1}^{k} \Re(\mathbf{r_i}) = 0, \quad \sum_{i=1}^{k} \Im(\mathbf{r_i}) = 0, \tag{19}$$

where k is the number of vectors in that loop. This way all displacements could be calculated, as well as the stresses using:

$$\sigma_{\max} = \frac{M(w/2)}{I_{\mathrm{z}}}, \tag{20}$$

where M is the bending moment in the flexure, calculated by multiplying K and the displaced angle θ, and w is the flexure width. To find the force required to actuate the whole mechanism at any point, Lagrange's equation was used. For static equilibrium (zero kinetic energy) this yielded:

$$\frac{\partial(V_{\mathrm{s}} + V_{\mathrm{f}})}{\partial q_{\mathrm{a}}} = F_{\mathrm{a}}, \tag{21}$$

where V_{s} is the potential energy of all (torsional) springs, V_{f} is the potential energy of all forces, F_{a} is the actuation force of interest and q_{a} is the generalised coordinate that describes the path traced by the actuation force. In our approach V_{f} was the sum of the potential of forces: $\mathbf{F_{GASs}}$ from the GASs pre-load, $\mathbf{F_{f,pawls}}$ from the friction of the attenuation stage pawls, and $\mathbf{F_{f,Y}}$ from the friction in point Y, all modelled as conservative forces. To calculate the potential energy of the pre-load from the pair of GASs, we added a constant force of 8.8 mN represented by the blue vector $\mathbf{F_{GASs}}$ in Figure 10 and multiplied it with the displacement of the shuttle. This force magnitude corresponds to the x-component of the reaction force when compressing a pair of GASs in the G6 accelerometer with 35 μm, obtained from the GAS model by [9] described in the Supplementary material Section 1.1. The potential energy of the friction force of the attenuation stage pawls, indicated by the orange vector $\mathbf{F_{f,pawls}}$ in Figure 10, was obtained by multiplying the force with the distance travelled of point Z'. This magnitude of this force will be determined in Section 12. Last, we obtained the potential energy of the friction force in point Y (vector $\mathbf{F_{f,Y}}$ in Figure 10) as the cross-product of vector $\mathbf{r_{M/Y}}$ with this force, multiplied by the angle difference $\Delta\theta_{M/Y}$ at full compression of the attenuation stage pawls. This meant that first the system had to be solved without the friction in point Y to obtain the normal force in point Y, after which the total actuation force F_{a} could be obtained.

2) *Ratchet-pawl:* Dimensioning was started by establishing the displacement that point Z should have according to requirement R4. Since previous versions of the accelerometers with anti-spring technology used ratchet-pawl combinations shifted 5 μm relative to each other with a tooth pitch of 10 μm, we decided to also use this configuration. This lowered the attenuation factor from 200 to 100 and the attenuation stage ratchet-pawl step-size from 10 to 5 μm according to requirements R3 and R4, and therefore saved footprint. Then, in order to obtain the displacement u_Z required to traverse 8 steps of 5 μm, the dimensions of the two ratchets were drawn schematically, shown in Figure 11. The starting position of both attenuation stage pawls was required to be removed from the ratchet by 3.4 μm according to constraint C2. Therefore, to avoid floating behaviour of the pawls, the first compression step was at 12.5μm. By adding 8 steps of 5 μm, the total distance the pawls at point Z should traverse was therefore 52.5 μm.

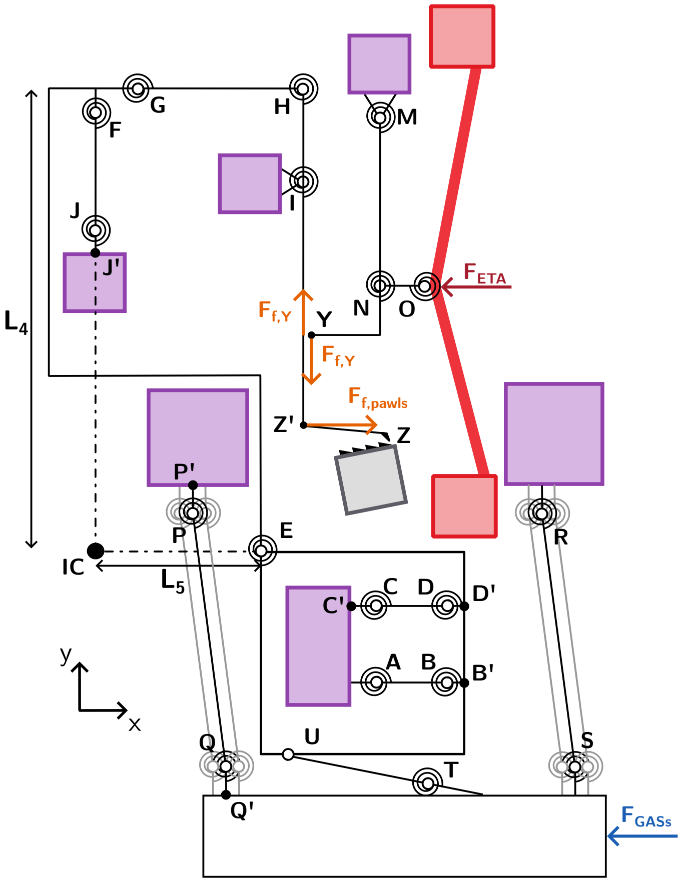

Fig. 10: An illustration of the PRB model of our design.

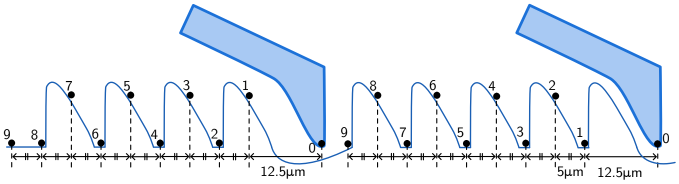

Fig. 11: An schematic illustrating the positions of the two attenuation stage pawls in each of the 9 positions.

3) *Attenuation stage:* We now started dimensioning the attenuation stage using the PRB model, as it would prescribe the force that the ETA should provide. To aid in the dimensioning, the design was also parametrically drawn in SolidWorks 2022. In order to minimise the actuation force of the ETA and thereby save footprint, all spring widths were set to their minimal value of 6 μm, as prescribed by constraint C2. As a starting point, length L_2 was set to 300 μm and all other flexure pivot lengths were set to 50 μm. The two springs with length L_1 were chosen to be 180 μm long and set apart by 230 μm based on a hand-calculation (see the Supplementary material Section 4.5.1) considering the buckling constraint C6. It became clear that to limit stresses and to reduce the actuation force at point Z, the whole height of footprint sections F1 and

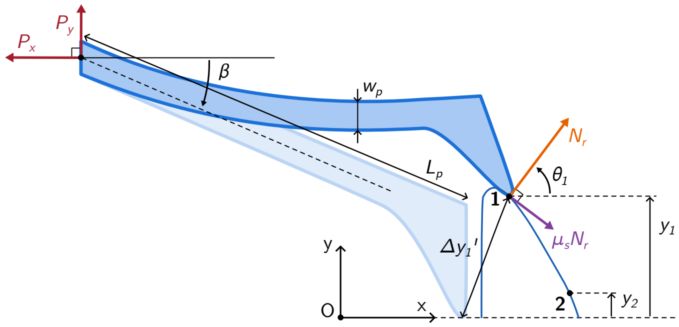

(a) A schematic diagram of the interaction between the ratchet teeth (light blue) and the pawl (dark blue). The light-blue pawl indicates the undeformed position in the absence of the ratchet.

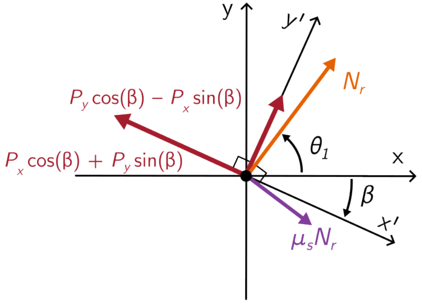

(b) The force vectors depicted together.

Fig. 12: An illustration of the force equilibrium on a pawl.

F2 (see Figure 9) should be used. This resulted in the choice for length L_4 of 1250 μm, and therefore length L_5 had to be 250 μm to obey the attenuation ratio of 5. Next, to allow the link connecting H and Z to be aligned with the y-axis to fit between the shuttle spring anchors, length $L_{\mathrm{G/H}}$ was chosen 200 μm, leaving roughly 100 μm for the thickness of link EG and the lengths of flexures G and H. Link HZ was now dimensioned to be as long as possible, resulting in lengths $L_{\mathrm{H/I}}$ and $L_{\mathrm{I/Z}}$ of 225 and 900 μm. Point Y was chosen as close to the the attenuation stage pawls as possible such that the displacement of the ETA to travel the 3.4 μm gap at point Y was minimised. Based on these coarse dimensions, the force to actuate the attenuation stage at point Y in the PRB model was approximately 1.4 mN at 52.5 μm and this value served as the starting point for the design of the ETA in Section IV-C5.

4) Friction from the pawl-ratchet contact: To determine the actuation force that the ETA should provide, the friction force from the attenuation stage pawls also had to be estimated. In Figure 12a the forces that act on one pawl with length L_p are shown, given a deflection of $\Delta y_1'$ perpendicular to the pawl resting on contact in point 1. Forces N and μ_sN represent the normal and static friction force respectively, and P_x and P_y are the reaction forces at the pawl end. Figure 12b shows the force vectors acting on the pawl when shifted together and where the reaction force vectors are expressed in coordinate system $x'y'$ that is aligned with the pawl. The three unknown force magnitudes N, P_x and P_y prescribed three independent equations to be solved. By applying static equilibrium in direction x$'$ and y$'$ the first two equations were found:

$$+\searrow \Sigma F_{x'} = 0:$$
$$-P_x\cos(\beta) - P_y\sin(\beta) + N\cos(\theta_1+\beta) + \mu N\cos(\pi/2-\theta_1-\beta) = 0, \qquad (22)$$

and

$$+\nearrow \Sigma F_{y'} = 0:$$
$$-P_x\sin(\beta) + P_y\cos(\beta) + N\sin(\theta_1+\beta) - \mu N\sin(\pi/2-\theta_1+-\beta) = 0, \qquad (23)$$

where the arrows indicate the positive directions. The third equation was found by recognising that the reaction force perpendicular to the pawl is equal to the stiffness of the beam k_p times deflection $\Delta y_1'$:

$$P_y\cos\beta - P_x\sin\beta = k_p\Delta y_1', \qquad (24)$$

with:

$$k_p = \frac{3EI_{p,z}}{L_p^3}, \quad \Delta y_1' = \frac{y_1}{\cos(\beta)} \qquad (25)$$

where $I_{p,z}$ is the second moment of area of the pawl with respect to the out-of-plane z-axis. Solving the three equations simultaneously the magnitudes P_{x}, P_{y} and N for each attenuation stage pawl could be obtained.

The static friction coefficient μ_s was assumed to be 0.75 based on the work of Wu et al. [18], who studied the friction in DRIE [110] sidewall surfaces for n-type single-crystal wafers.

To assume a worst case, reaction forces P_x and P_y were calculated for the situation where both attenuation stage pawls are resting on a ratchet tooth; point 1 being the highest position before angle θ_1 starts to increase rapidly, and point 2 being 5 μm apart from point 1 along the x-axis. It was also assumed that the pawl tips would be at rest at the base of the ratchet teeth at y=0. Using the values listed in Table V with a Young's modulus of 169 GPa yielded values for P_{x} and P_{y} at point 1 and point 2 of [2.4, -0.1] and [1.9, 0.3] mN respectively, totalling 4.3 mN for force P_{x}. To verify the plausibility of this result, reaction force P_x was also calculated for the pawls connected to the shuttle of accelerometer version G5 from [9]. For a pawl width of 6 μm and out-of-plane thickness of 50 μm while using the same length L_{p} and angle β, this yielded a total force P_{x} for both points of 2.2 mN. Since two sets of pawls are connected to the shuttle the total force equals 4.4 mN. Therefore, considering that the ETA that pushes shuttle was designed to provide 18 mN while approximately 10 mN is required to compress the anti-springs and 4 mN to displace the shuttle springs, this seemed a reasonable value. For this reason we had confidence that our approach gave a good approximation of the attenuation stage pawl friction forces.

5) Electro-thermal actuator: To design the ETA we used the same approach as [9] to numerically model the work on V-beam ETAs by Enikov et al. [19]. Using the SciPy `solve_bvp` function, equation [9, eq. (3.6)] was solved with boundary conditions [9, eqs. (3.8)-(3.10)]. This yielded the average temperature difference ΔT and longitudinal load P_0, given an external force F and a displacement of the ETA shuttle d_{ETA}. For the thermal expansion coefficient Equation 3 was used. Next, an estimation of the force that the ETA should provide at point Y was made, being the sum of the force required to deform the flexural elements and the friction forces emerging from the sliding contacts. Since the the dimensions of the actuator stage were still unknown, it was estimated that to actuate all flexures from point Y would require ∼2 mN based on the 1.4 mN that was determined for the attenuation stage in Section IV-C3. Considering the friction forces, three contact interfaces were identified that would add to the required actuation force of the ETA: two attenuation stage pawl-ratchet contacts at point Z and one contact at point Y in Figure 8. Because the dimensions of the actuator stage could not yet be determined, being dependent on the dimensions of the ETA, only the friction force $\mathbf{F}_{\mathrm{f,pawls}}$ from the two pawl-ratchet contacts were used in the dimensioning of the ETA. Also, the component of friction force $\mathbf{F}_{\mathrm{f,Y}}$ to add to the required ETA actuation force was estimated to be small compared to the contribution of force $\mathbf{F}_{\mathrm{f,pawls}}$ given its direction. Therefore, adding 4.3 mN from force vector $\mathbf{F}_{\mathrm{f,pawls}}$, derived in Section IV-C4, to 2 mN the total actuation force estimate at point Y yielded 6.3 mN. Then, by combining the displacement in point Y that corresponded to this minimum load, which is 49.2 μm plus an additional 3.4 μm to cross the gap, the work that the ETA should do was obtained by taking the product between 6.3 mN and this displacement. Therefore, depending on the fraction of dimensions $L_{\mathrm{M/N}}$ and $L_{\mathrm{M,Y}}$ in y-direction, the ETA could either provide a high force with low displacement, and vice versa. By plotting the force-displacement relationships as a function of the average ETA beam temperature from the thermo-mechanical model, the design space could be visualised.

Considering the buckling limit from Equation 6 on the longitudinal force P_0 in the ETA beams and a maximum average temperature of 530 K (adopted from [9]), it became clear that the ETA required many beam-pairs and should therefore be located in footprint section F3. This limited the ETA beam length to 410 μm when the ETA anchors and ETA shuttle width $w_{\mathrm{s,ETA}}$ were taken to be 90 μm and 30 μm wide respectively. In x-direction initially 400 μm was allocated to the ETA, leaving ∼300 μm for the rest of the actuator stage.

TABLE V: A list of all relevant dimensions of the attenuation stage ratchet-pawl.

Name	Symbol	Value
Pawl length	L_{P}	[CONFIDENTIAL]
Pawl width	w_{P}	[CONFIDENTIAL]
Pawl angle	β	[CONFIDENTIAL]
y-coordinate of point 1	y_1	[CONFIDENTIAL]
y-coordinate of point 2	y_2	[CONFIDENTIAL]
Ratchet tooth inclination at point 1	θ_1	[CONFIDENTIAL]
Ratchet tooth inclination at point 2	θ_2	[CONFIDENTIAL]

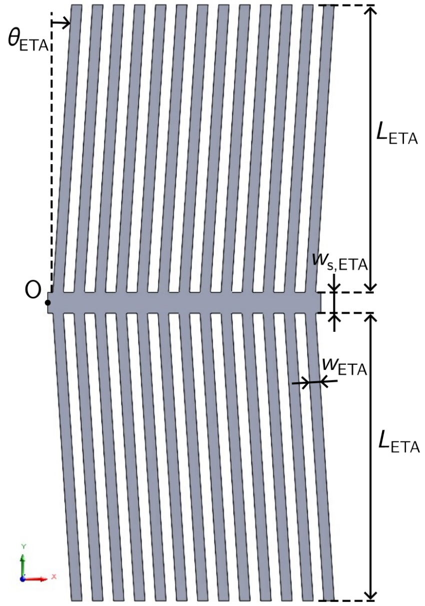

Fig. 13: The designed ETA with all relevant parameters indicated.

In our analysis, we investigated ETA beams with widths of 10 μm, 15 μm, and 20 μm. With a consistent beam spacing of 15 μm between each beam, we could therefore accommodate 16, 13, and 11 beams within the allocated footprint for the respective widths. For each beam width, the beam angle was also varied to find configurations that would fall within the constraints. Since the buckling limit of flexure combination N and O was not yet known, we looked for operating points with the largest displacement d_{ETA} as it would reduce the actuation force. A beam width of 15 μm with an angle θ_{ETA} of 3.7° was eventually chosen as this appeared to give the largest displacement. This design configuration is shown in Figure 13 with its force-displacement contour plot in Figure 14, where the red curve indicates the temperature constraint, the magenta curve indicates the buckling constraint of the ETA beams with a factor of safety of 3 and the blue curves represent the points that provide the work required to fully compress the whole mechanism. The working point is indicated by the black dot at a displacement of 8 μm. An overview of the plots for the different ETA beam configurations that led to this design choice can be found in the Supplementary material Section 4.5.2.

6) Actuator stage flexures: Based on the obtained displacement for the ETA at point O of 8 μm, the links and flexures of the actuator stage could be dimensioned. Like before, flexure pivots (M, N and O) were again initially given a length of 50 μm and lengths $L_{O/N}$, $L_{N/M}$ and $L_{M/Y}$ were chosen such that an 8 μm displacement of the ETA would allow the attenuation stage pawls to reach the last ratchet-tooth.

D. Dimensioning, phase 2

Now that all dimensions of the mechanism were roughly known, the whole mechanism was modelled in the SolidWorks

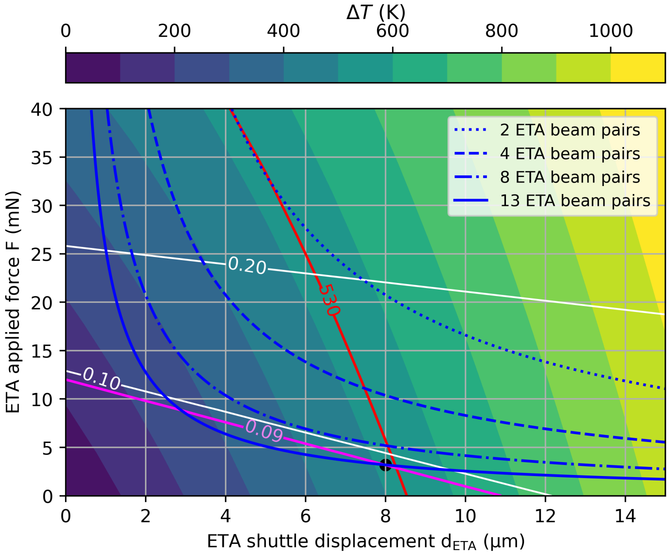

Fig. 14: A contour plot of the average temperature increase in the electro-thermal actuator (ETA) beams as a function of the ETA shuttle displacement d_{ETA} and load F_{ETA}. Width w_{ETA}: $15\mu\mathrm{m}$ and angle θ_{ETA}: 3.7deg. The red curve indicates the temperature constraint, the magenta line indicates the buckling constraint of the ETA beams and the blue curves indicate the points that provide the work required to fully compress the whole mechanism. The white curves indicate the longitudinal force P_0 in each ETA beam.

2022 CAD software and analysed using FE analysis in ANSYS Mechanical R2022 to verify the stresses and displacements.

1) Finite Element model of the mechanism without the ETA: The input for the FE simulations were the CAD models shown in Figure 15 and 13. A 2D plane-stress static structural analysis was used for both models, but due to limitations of the software we had to split up the analysis into two pieces, their boundary indicated by the red dashed line in Figure 15. These pieces will be referred to as segment O-U and segment U-shuttle, named after their respective in- and output points. Segment U-shuttle was analysed first to obtain the attenuation factor between the motion transfer of point U and the shuttle. All anchor points were given the Fixed Support boundary condition, including the ends of the GASs where it would connect to the proof-mass. Then the shuttle pawl end (point U) was moved a distance of 35 $\mu\mathrm{m}$ in positive x-direction using a Remote Displacement boundary condition and then displaced downward in negative y-direction. The output displacement of the shuttle in x-direction and the reaction force at point U were recorded. To model segment O-U all anchor points were again assigned the Fixed Support boundary condition. On point U the reaction force from segment U-shuttle was applied and the friction force from the attenuation stage pawl contact points Z_1 and Z_2 of 4.3 mN (derived in Section IV-C4) was added as a follower force in point Z', with the direction obtained from the PRB model. For the friction in point Y, a static friction coefficient of 0.75 was used, the same value used in Section IV-C4 from [18]. Due to convergence issues, the friction forces on both sides of the contact in point Y were manually applied using the Force boundary condition and the sliding of the contact was achieved using the Frictionless Support contact type. To obtain the direction and magnitude of these friction forces, we first solved the model without friction and recorded the normal force in point Y, the friction force vectors were then calculated using the PRB model. Point O was now given a displacement of 8 $\mu\mathrm{m}$ using a Remote Displacement boundary condition and the reaction force was recorded for later use in the FE ETA model. For the determination of the attenuation factor, we gave point Z_1 a displacement of 52.5 $\mu\mathrm{m}$ and recorded the output displacement of point U in negative y-direction. Both segments used the orthotropic material model from Table II and were rotated 45° in counter clockwise direction to align the global x-axis with the [110] silicon crystal direction.

2) Finite Element model of the ETA: The ETA was modelled last as the reaction force in point O from segment O-U served as a boundary condition on point O on the ETA shuttle (see Figure 13). To accurately capture the behaviour of the ETA at high temperatures we used temperature dependent material properties for the thermal expansion, thermal conductivity, resistivity and the Young's modulus. For the coefficient of thermal expansion the same equation was used as in Section III (Equation 3). Since the work of Ohishi et al. [20] demonstrated a strong dependence of the thermal conductivity on the silicon doping level, we tried to obtain the values that would match the level of doping in our device layer by interpolating their data. Given that the resistivity of our silicon wafer was reported to be between 5 and 10 $\mathrm{m}\Omega\cdot\mathrm{cm}$, the corresponding boron concentrations could be derived using the work of [21]. This yielded a lower and upper bound of $8.5\cdot10^{18}$ and $2.1\cdot10^{19}\ \mathrm{cm}^{-3}$ respectively. We then estimated the thermal conductivity values using an average concentration of $1.5\cdot10^{19}\ \mathrm{cm}^{-3}$ by linearly interpolating the data from [20, Fig. 3(c)]. Because data above 770 K was limited, the thermal conductivity data of intrinsic silicon (no doping) was also used from [22] as a guideline for our estimation. The result of this can be found in the Supplementary material Section 4.6.1. The temperature dependence of the resistivity is also described in the Supplementary material (Section 4.6.2). Last, the temperature dependence of the Young's modulus in the [110] direction was adopted from the work of Ono et al. [23], being:

$$E_{[110]} = 1.51\cdot10^{5}\ e^{(2.7\cdot10^{-3}(\mathrm{eV})/(k_{\mathrm{B}}T))}\ (\mathrm{MPa}), \qquad (26)$$

where k_{B} is the Boltzmann constant and T is the temperature in Kelvin. Based on the temperature dependent material properties, a thermo-mechanical and thermo-electric FE model were built: the thermo-mechanical model working with an average ETA temperature as input and the thermo-electric model working with an applied current. Then both the numerical and FE models of the ETA were validated using the work of Zhu et al. [24] that can be found in the Supplementary material

Section 4.6.3. To verify that the (out-of-plane) sag due to gravity at any point in the mechanism does not exceed 5 μm (constraint C7) we finally performed a 3D FE analysis, using a silicon density of 2300 $\mathrm{kg/m^3}$.

3) Mesh convergence: For each of the described models, a mesh convergence study was performed using PLANE183 elements with geometric non-linearity enabled by incrementally decreasing the mesh size and recording the maximum principal stress. The results of this study can be found in the Supplementary material, Figure 17. For segment O-U and U-shuttle 120k and 50k elements were used respectively to ensure mesh convergence, defined as $<$1% change, was achieved. For the sag analysis we used 25k SOLID187 (3D 10-node tetrahedral structural solid) elements, including geometric non-linearity. The ETA was simulated using roughly 30k PLANE183 elements.

4) Iterative process: To reach a design that adhered to all constraints and requirements, we used an iterative process where parameters such as the flexure and link lengths were manually adjusted through trial and error. In this process we converted link GH to combine into one long flexure to limit the stress at point H, from now on referred to as flexure GH. The PRB model was therefore adjusted according to the PRB model of a long flexure with combined force-moment end loading with a characteristic radius factor γ of 0.85 [16, Fig. Fig. A.5.9]. All relevant dimensions of the final version of the design can be found in Table VI.

V. EXPERIMENTAL VALIDATION

After finishing the dimensioning of the design including verification the PRB model with FE analyses, a scaled prototype was manufactured to validate both models with experimental data.

TABLE VI: A list of all the relevant dimensions of the attenuation and actuator stage.

Name	Symbol	Value
Flexure length	L_1	180 μm
	L_2	300 μm
	L_3	488 μm
	L_4	250 μm
	L_{GH}	207 μm
	L_{E}	30 μm
	L_{I}	75 μm
	L_{M}	65 μm
	L_{N}	85 μm
	L_{O}	50 μm
Link width	w_{EG}	50 μm
	$w_{\mathrm{HZ'}}$	50 μm
	w_{MY}	80 μm
Width of all flexures	w	6 μm

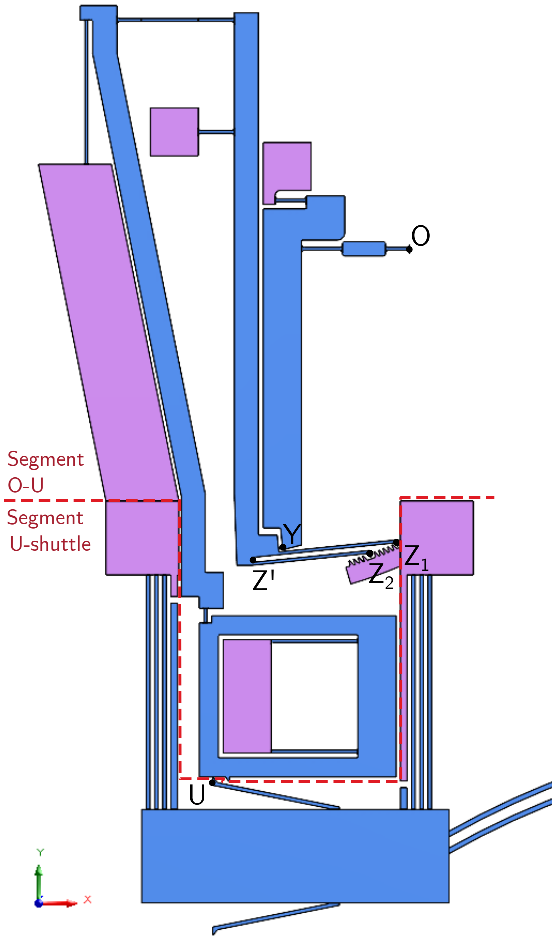

Fig. 15: A screenshot of the CAD model made using SolidWorks 2022. The purple colored parts are the anchor parts and the blue colored parts are the floating parts and can move freely. Point O is the attachment point of the ETA shuttle, point Y is the point of sliding friction, point U is the shuttle-pawl end (here the shuttle shown in uncompressed state), point Z' is the center point between both attenuation stage pawls and Z_1 and Z_2 indicate the pawl ends.

A. Prototype manufacturing

The materials that were selected to build the prototype with were acrylic plate (PMMA) for most rigid parts and stainless spring-steel strip types 1.1274 and 1.4310 for the flexures, with Young's moduli of 210 and 185 GPa respectively. This was done because the material properties of the acrylic plate were unknown and would therefore add extra uncertainty to our validation. However, to ease manufacturing, we decided to make the shuttle pawl out of acrylic as well because we expected an uncertainty in stiffness of this pawl to only have a small effect on the results. Also, since manufacturing the GASs using steel strips would pose significant challenges, the GASs pre-load was instead established by increasing the spring width of the shuttle springs. Both in-plane and out-of-plane scaling factors were chosen in such a way as to keep the

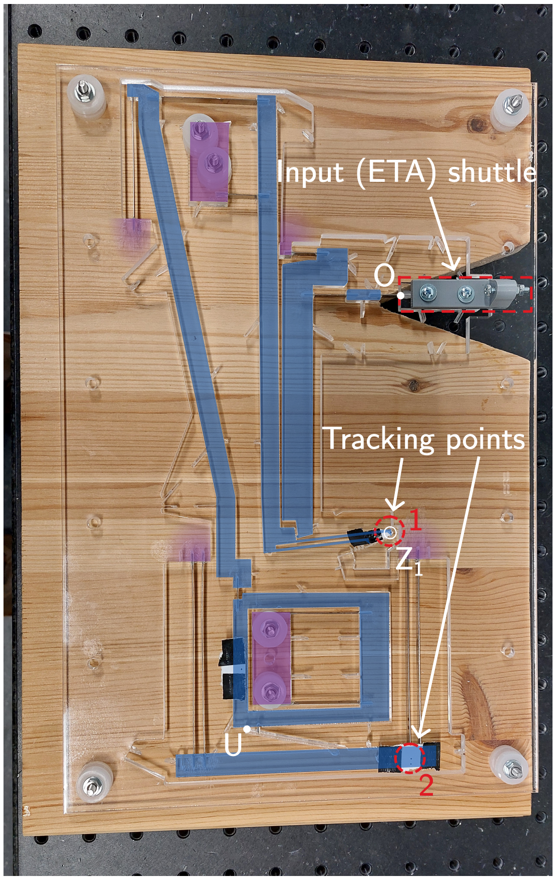

Fig. 16: A picture of the prototype with the floating structures colored in blue and the anchors colored in purple. The tracking points on the paper pieces are indicated by the red circles.

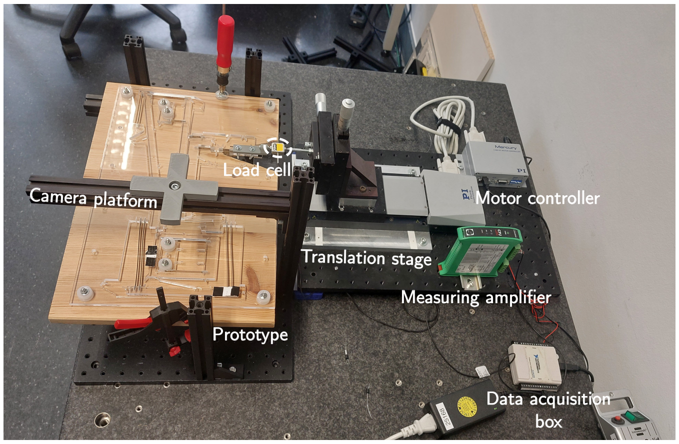

Fig. 17: A picture of the measurement set-up where each relevant component is annotated.

same relative stiffnesses between the rigid parts and flexures, given the thicknesses that were available for the materials. This meant that for any flexure k the following relation should hold:

$$E_{\text{PMMA}} I_{\text{z},k,\text{PMMA}} = E_{\text{steel}} I_{\text{z},k,\text{steel}}, \tag{27}$$

where I_{z} is the second moment of area of the flexure around the out-of-plane z-axis. Rewriting the second moment of area ($I_z = \frac{tw^3}{12}$) in terms of the in-plane and out-of-plane scaling factors S_{ip} and S_{ip} resulted in:

$$E_{\text{PMMA}}(S_{\text{op}} t_{\text{k,Si}})(S_{\text{ip}} w_{\text{k,Si}}^3) = E_{\text{steel}} t_{\text{k,steel}} w_{\text{k,steel}}^3, \tag{28}$$

where $w_{\text{k,Si}}$ and $t_{\text{k,Si}}$ are the width and height of the silicon flexure, and $w_{\text{k,steel}}$ and $t_{\text{k,steel}}$ are the width and height of the steel flexure. In other words, any steel flexure should have the same stiffness had the flexure been made of PMMA. Assuming 5 mm thick acrylic ($S_{\text{op}} = 50$) with a Young's modulus of 2.9 GPa and a silicon flexure width of 6 μm, this resulted, for an in-plane scaling factor S_{ip} of 200, in a 99.6% match between the left- and right-hand side of Equation 28 if we used a 1.4310 steel flexure with a 5 by 0.3 mm cross-section. We therefore decided to use these two scaling factors in our prototype. Now, to include the pre-load of the GASs into the shuttle springs of the prototype, we calculated the pre-load with the GAS model (Supplementary Material Section 1.1) using the recently obtained scaling factors, again assuming a PMMA Young's modulus of 2.9 GPa. Then we looked for combinations of steel flexures that would match this pre-load when the shuttle would be fully compressed at 7 mm (200 times 35 μm). A 99.5% match was found by using four 0.5 mm wide 5.0 mm high 1.1274 steel flexures. The rigid parts were then cut out of the acrylic plate using a laser cutter, leaving slits for the insertion of the steel flexures. Support beams were in place to temporarily connect the rigid parts to ease gluing the flexures in the slits, to be cut through afterwards. The ratchet for the attenuation stage pawls was cut separately to make it removable. We then manufactured the flexures by hand using a guillotine shear and a flat metal file. Last, after measuring the height of each flexure, we glued the flexures into the slits using two-part epoxy Permabond ET 5428. The measured average heights can be found in Table VII, where the height of springs with length L_1 and L_3 are numbered from top to bottom and left to right. The width of the shuttle pawl was also measured and is included in the table. The acrylic plate was then mounted on a wooden back plate to support all the anchor points and a 3D printed (shuttle) part was attached for the connection between the test stage and point O. White pieces of paper with black dots were taped to point Z_1 and to the shuttle to serve as tracking points for the recording of the displacements. The whole prototype can be viewed in Figure 16

B. Measurement set-up

The measurement set-up consisted of a frame of 25x25 mm Thorlabs profiles on top of which the prototype was clamped (see Figure 17). A load cell (FUTEK LSB200 FSH03875) was connected between the translation stage (PI M505.4DG), driven by a PI Mercury C-863 motion controller, and point O to record the reaction force. The data from the load cell was sent trough a measuring amplifier (Scaime CPJ) to a data acquisition box (National Instruments USB 6008) . To measure the displacements of the tracking points indicated in Figure 16 we used a 64 MP (Samsung A52s 5G) camera placed on top of the camera platform 11 cm above the prototype. The tracking point on the camera footage was then tracked using the Tracker software (version 6.1.6) from the OSP collection [25].

C. *Measurement method*

In order to validate PRB and FE model we first measured the force-displacement characteristic at point O by giving a displacement to the translation stage of 2 mm. This measurement was repeated 10 times to be able to see the effect of random errors and for every measurement we re-engaged the shuttle pawl into its pre-loaded position. Next, we applied a step-wise displacement to point O with increments of 0.2 mm and recorded the displacement of tracking point 1 using our camera with 5x magnification, waiting ~2 s in every step before going to the next step. The same process was repeated while recording the displacement of the shuttle at tracking point 2, this time with 10x magnification and waiting ~10 s in every step. An example of the tracked data for both tracking points is shown in Figure 18, where the 10 steps can be distinguished. As the measure for the true displacement in each step we used the median of all data points in that step. To ensure that the PRB and FE models would use the correct pre-load, we measured the compression distance by tracking the shuttle displacement while engaging and disengaging the shuttle pawl 10 times. This yielded a compression distance of 6.8 mm, 3% less than the nominal compression distance of 7 mm. It should be noted that in all measurements the ratchet part was left out as we had been unable to include it in an accurate manner in our FE or PRB model.

TABLE VII: A list of all measured flexure dimensions of the prototype.

Parameter	Symbol	Value
Spring height	$t_{3,1}$	5.13 mm
	$t_{3.2}$	5.03 mm
	$t_{3,3}$	5.00 mm
	$t_{3,4}$	5.03 mm
	$t_{1,1}$	5.05 mm
	$t_{1,2}$	5.05 mm
	t_2	5.15 mm
	t_{GH}	5.1 mm
	t_{E}	5.0 mm
	t_{I}	5.2 mm
	t_{M}	5.2 mm
	t_{N}	4.9 mm
	t_{O}	5.2 mm
Width of the shuttle pawl	w_4	1.5 mm

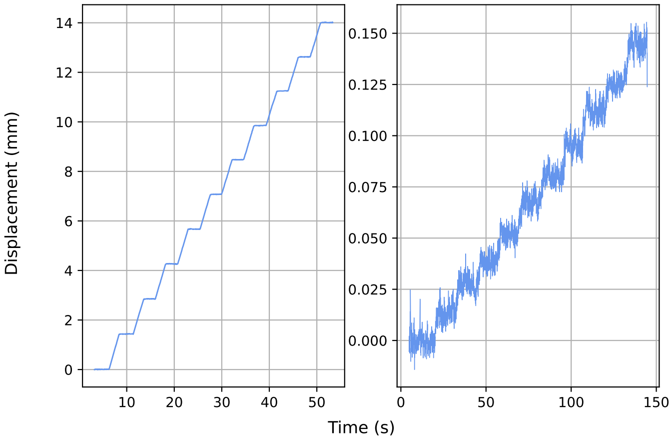

Fig. 18: One recording of the tracked displacements of the shuttle at tracking point 1 (left) and the attenuation stage pawl at tracking point 2 (right).

In order to verify that displacing point O of the prototype and measuring the displacement of point Z_1 would give similar results when point Z_1 would be displaced and left to rest on the ratchet, we conducted force-displacement measurements to obtain the stiffness of one attenuation stage pawl, reported in the Supplementary material Section 5.1.

VI. RESULTS

A. *Micro-scale silicon design*

The geometric advantage (GA), defined here as the input displacement at point Z_1 divided by the output displacement of the shuttle, is plotted for each of the eight compression steps in Figure 19 for both the PRB model and the FE model. Since the displacement steps of segment U-shuttle did not match with the actual steps of the attenuation stage pawls, we interpolated this data for the calculation of the the GA. The yellow line and the yellow colored area indicate the nominal value and tolerance of requirement R4 respectively. Both models lie within this area and therefore fulfill this requirement. Because the steps-size of the attenuation stage pawls is 5 μm this means also requirement R3 is automatically met. The minimum and maximum compression step-sizes predicted by the FE model are 50 nm and 54 nm, respectively, and 51 nm and 52 nm by the PRB model.

To find the required displacement at point O to reach a full compression of 52.5 μm at the the attenuation stage pawls, we applied a displacement to the PRB model and the FE model at point O and recorded the displacement at point Z_1. The result can be viewed in the Supplementary material Figure 21, where it appears that the maximum compression is reached at a displacement of point O of 7.9 μm for both models. At the same time the reaction force was recorded, this is shown in Figure 20. For a 7.9 μm displacement the PRB and FE models predicted 54.0 and 54.7 mN respectively. At this point the buckling in the flexures with length L_1 and the flexures at point O and N were verified. The maximum reaction force in the

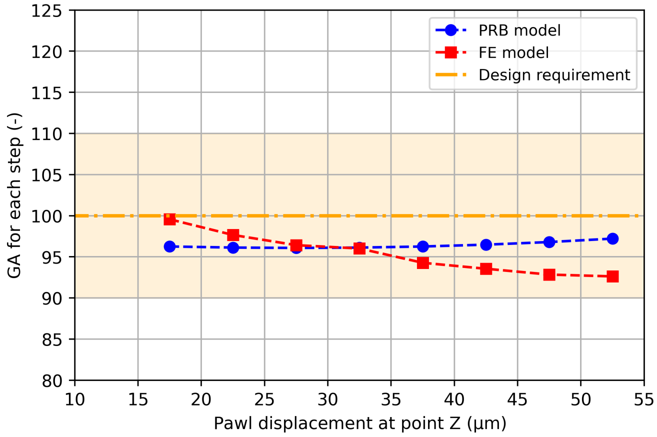

Fig. 19: The displacement of the attenuation stage pawls at each compression step of the micro-scale silicon design plotted against the GA for that step. The ±10% margin for design requirement R4 is shown indicated by the yellow colored area.

lower flexure with length L_1 according to the FE model was 19.4 mN, therefore within the limit derived from constraint C6 of 30.9 mN. To calculate the critical buckling load of the combination of the flexures at point O and N, we treated them as one long flexure. Then, the critical buckling load of this (50 + 85 =) 135 μm long and 6 μm wide flexure was calculated using Equation 6 to be 164.7 mN. Considering the safety factor of three from constraint C6 this resulted in a critical load of 54.9 mN. Since the maximum force in point O was recorded to be 54.7 mN in the FE model, the constraint was complied with.

To assume a worst case, the reaction forces from the FE model at 7.9 μm at point O were subsequently used as the input for the numerical and FE thermo-mechanical ETA models. Due to a failing convergence of the FE thermo-electric model, only the thermo-mechanical FE model could be evaluated. The result is shown in Figure 21 where it can be observed that for both models the maximum compression at 7.9 μm is reached within the maximum temperature constraint of 530 K. This indicates a fulfillment of requirements R1 and R2. The outcome of the FE analysis where the sag was investigated can be found in the Supplementary material Section 5.4. According to the model, the maximum sag was 0.24 nm, well within the 5 μm prescribed by constraint C7.

B. Macro-scale prototype

After processing the data of both tracking points, we linearly interpolated all data points to match with the the actual attenuation stage pawl steps. Calculating the GA in each step then yielded the results in Figure 22. The interquartile range (IQR) and the mean of the 10 data points are plotted to indicate the spread of the interpolated measurement data. The yellow line and the yellow colored area again indicate the nominal values and tolerances of requirements R3 and R4. The results of the PRB and FE models are also shown. For the FE model

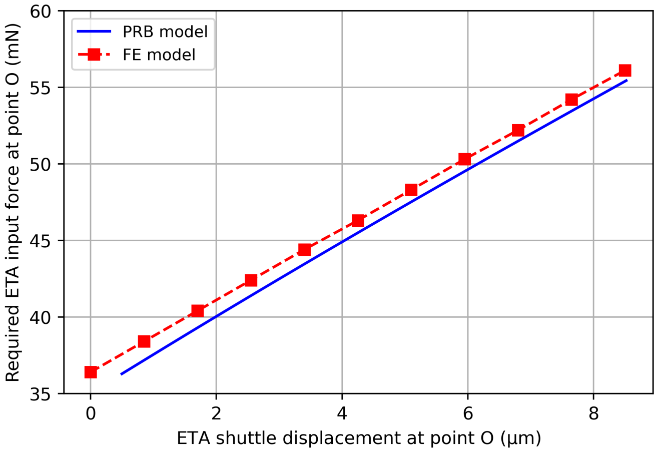

Fig. 20: The required ETA input force plotted against the ETA shuttle (input) displacement.

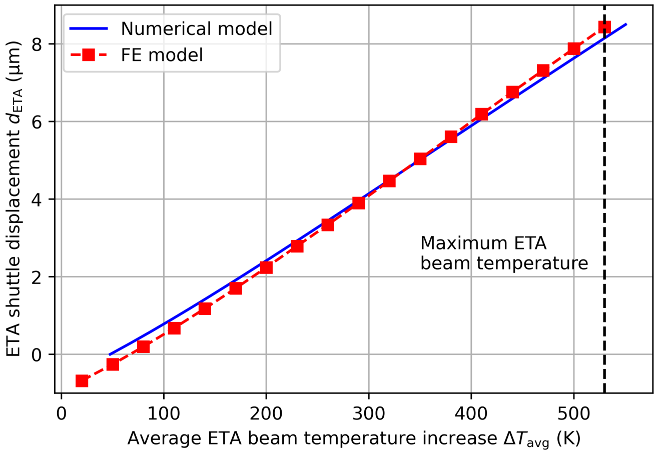

Fig. 21: The ETA shuttle displacement plotted against the average temperature increase of the ETA.

a sensitivity analysis was performed to investigate the effect of the uncertainty of the Young's modulus of the PMMA on the results. For both a lower and upper limit of the Young's modulus of 2.76 and 3.30 GPa, reported in [26], we ran the same FE simulations. In the figure these results are included as error bars for the FE model data. To examine the effect that replacing the GASs with thicker shuttle-springs had on the result, a FE simulation that included PMMA GASs was carried out as well and its result is included in the figure.

The measured force-displacement data are displaced twice in Figure 23 to thoroughly compare them to the PRB and FE models. In the figure all 10 measurements are overlaid on top of each other including their average slope, calculated using NumPy's `polyfit` function with degree 1. Like before, we performed a sensitivity analysis with the FE model to show the influence of the uncertainty of the PMMA, indicated by the error bars. Another uncertainty that was investigated was the dynamic coefficient of friction of the PMMA. In [27,

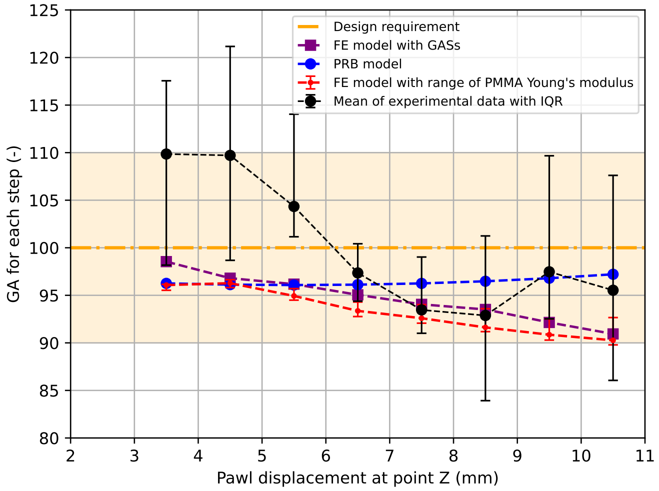

Fig. 22: The displacement of the attenuation stage pawls at each compression step of the macro-scale prototype plotted against the GA for that step. The ±10% margin for design requirements R3 and R4 is shown indicated by the yellow colored area.

Fig. 7], for a sliding velocity roughly 3 mm/min, the lower and upper bound of the dynamic coefficient of friction were approximately 0.2 and 0.5 respectively. We therefore added the outcomes of both models for these friction values to indicate the sensitivity to this uncertainty. Regarding the attenuation stage pawl stiffness, the average stiffness we measured was 15.1 N/mm (see Supplementary material Section 5.1), and, together with the normal force in point Y at maximum compression of 0.29 N from the FE model, the deformation of the pawl was estimated to be (0.29 N/15.1 N/mm =) 0.02 mm. Because this value is about 2% of the pitch of the ratchet teeth, this effect was neglected in our analysis of the GA since the variation of the measured shuttle output displacement seemed to have a much larger effect on the GA when looking at Figure 22.

VII. Discussion

In this work we designed a novel mechanism that is able to fine-tune the compression distance of the GASs in the Innoseis accelerometer version G6 with the goal to potentially compensate the TDB. After a rigorous process of verification and validation, our results give us confidence that our design meets all requirements that were formulated on the basis of our TDB analysis. While previous research has focused on electrostatically modifying the pre-load of GASs [8], we have demonstrated in this work the feasibility of doing this mechanically without requiring a continuous energy supply into the system. It should be noted, however, that our presented method of fine-tuning the GASs can not be used to modify the pre-load in response to temperature changes as the modification of the pre-load is irreversible due to the ratchet-pawl mechanism. To compensate any TDB, one therefore needs to first measure the TDB, then compress specific GASs with our proposed mechanism, and last measure the TDB again to track the effect. The irreversible nature of our mechanism requires this to be done in an iterative manner. Nonetheless, the possibility of fine-tuning the GASs could still potentially prove to be a valuable tool as was demonstrated by our TDB model.

In the verification process of our micro-scale silicon design, the PRB model and the 2D FE model showed good agreement in Figure 19, indicating the that requirements R3 and R4 were met. Likewise, we were able to verify the force and displacement input parameters of the ETA model (Figure 20, and Figure 21 in the Supplementary Material) and subsequently the numerical and FE ETA models themselves in Figure 21. This indicated fulfillment of requirements R1 and R2.

In the validation of the PRB and FE models with the experimental data of the prototype, we observed reasonable alignment in Figure 22. However, especially at the lower attenuation stage pawl displacements, some deviation was visible. The relatively large variation of the experimental data mean and IQR compared to the model data seems to indicate that not enough measurements were performed to average out random effects like vibrations. Also, since all models were either 1D (PRB) or 2D (FE), out-of-plane effects could contribute to this deviation. The sensitivity analysis of the FE model with the Young's modulus of the PMMA seemed to only have a small effect, which implies that it probably plays a minor role in the observed difference with the experiments. Finally, the results from the FE model that included the GASs closely matched the results of the FE model without the GASs, suggesting that our prototype, in which the GASs pre-load was mimicked by the use of thicker shuttle springs, represents the GAS pre-load well.

The validation of the force-displacement of point O shown in Figure 23 reveals that both models (left and right) approximate the experimental data well when comparing the average slope with the zero friction model data. The PRB model, however, shows an offset in the beginning of the graph in both axes. The offset in the x-axis can be explained because the PRB model is solved for the initial condition where the attenuation stage pawls have zero displacement, giving point O a non-zero initial displacement. This is also visible in the result of the small-scale silicon design (Figure 20). It is not obvious what causes the offset in the y-axis, but because a similar offset was visible in the results from Figure 20 it suggests that the PRB model has some systematic error in predicting the real-world behaviour. An interesting observation is that the sensitivity analysis of the friction coefficient presents opposite results: the hysteresis in the PRB model matches the measurements the closest for a friction coefficient of 0.2, while a friction coefficient of 0.5 shows the best match in the FE model. This seems to indicate that at least one of the models must have some error in the calculation of the influence of the friction force in point Y. As was observed for the variation of the Young's modulus of the PMMA in Figure 22, in the force-displacement curve of the FE model the effect again is rather small which strengthens our suspicion that its effect only has a small effect on our validation.

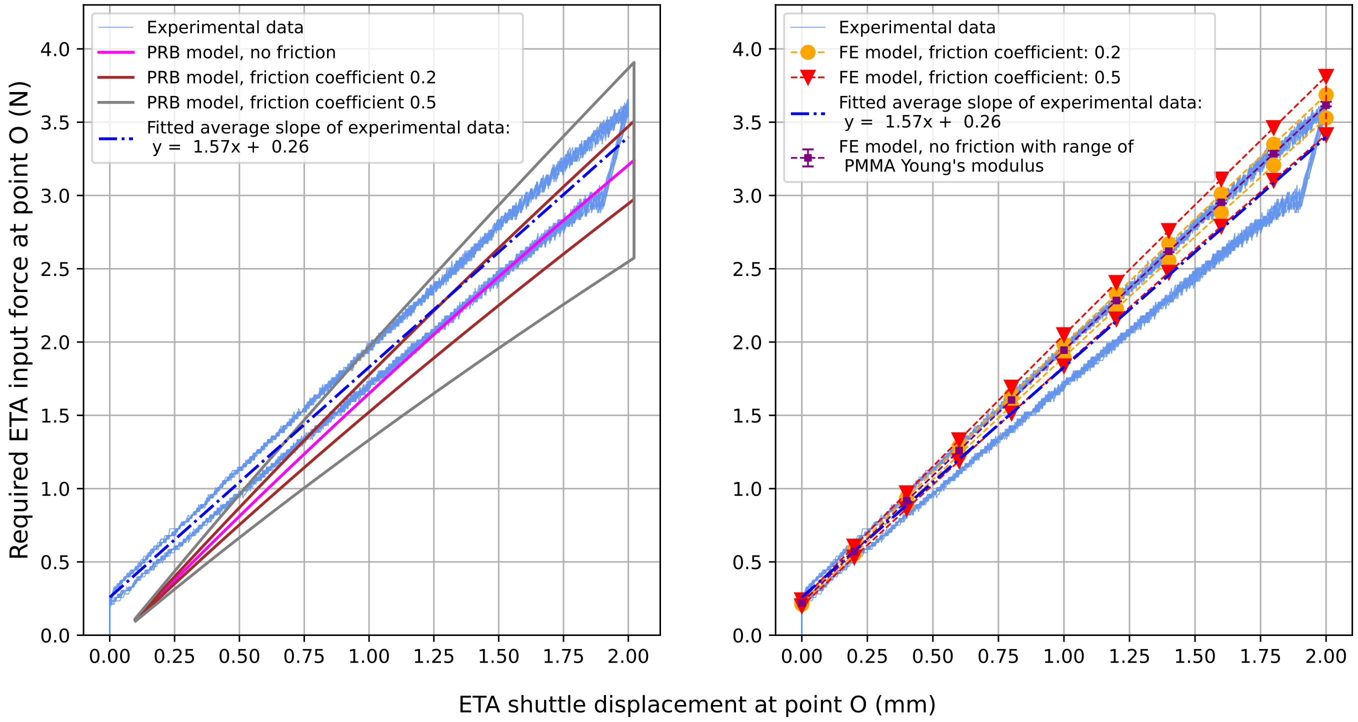

Fig. 23: The experimental data of the force-displacement characteristic at point O of the macro-scale prototype plotted together with the PRB model (left) and the FE model (right).

Although the results from our verification and validation show promise for our mechanism, there are some limitations that need to be underlined. First of all, in the experiments the ratchet (at point Z) was omitted and the friction from the attenuation stage pawls is therefore still a source of uncertainty. Second, because the static friction coefficient of 0.75 that we applied in our calculations was adopted from [18], who determined it for a silicon n-type DRIE [110] sidewall surface, there could be some error in our model predictions since our wafer is differently doped (p-type) [28] and our friction surfaces do not all align with the [110] direction. DRIE process parameters have also been shown to have a large influence on the static friction coefficient [29], adding to the uncertainty.

Third, because we used a rough estimate of the maximum tensile stress (i.e. fracture strength) in our stress constraint C5, it might overestimate the true value of the maximum stress that our mechanism can endure. In [30] it was demonstrated that having a thicker device layer can lower the fracture strength, presumably because of increased surface roughness in the bottom region of the device layer. For this reason, with the absence of surface roughness data from our own manufacturing process, this uncertainty needs to be addressed before manufacturing. Another issue that has limited our design verification is the failing mesh convergence of our thermo-electric FE ETA model. Consequently, by relying solely on the average temperature increase as the input parameter, our analysis may overlook more complex dynamics of the ETA operation, suggesting a need for an improved thermal model. One last limitation of the approach we used was that the TDB model could not be validated, which makes the usability of our mechanism to compensate TDB therefore uncertain.

To prove the usability of our mechanism in compensating the TDB, future research should first focus on validating that the minima we observed in the results from our TDB model (Figure 7) indeed exist. Additionally, it should be investigated that our method of compensation would also work for the non-symmetrical case since each spring can have a different width as a result of the manufacturing variations. Lastly, we recommend validating our method for estimating the ratchet-pawl friction forces as it determines for a large part the requirements of the ETA.

VIII. CONCLUSION

The goal of this work was to design a mechanism that can fine-tune the compression distance of the GASs in the Innoseis G6 accelerometer to be able to potentially compensate the TDB. We first modelled the TDB to serve as the basis of our requirements, after which we designed our mechanism using a combination of pseudo-rigid body and finite element modelling. To validate these models we manufactured a macro-scale prototype from PMMA and spring steel. The measurements on the geometrical advantage between the attenuation stage pawls and the shuttle showed a relatively large spread of the mean but for the most part they aligned well with our model predictions.

There was also good agreement in the force-displacement relationship with our PRB and FE models. However, in the sensitivity analysis of the friction coefficient, the PRB model showed a much stronger dependency on the friction coefficient than the FE model, indicating a flaw in one or both models. This adds uncertainty to the predicted ETA actuation force of the micro-scale design, and, for the feasibility of our proposed mechanism, should therefore be investigated further. We successfully validated the models we used to design the ETA by replicating data from literature. All in all we can conclude that our design meets the requirements to compress the GASs in the Innoseis G6 accelerometer without requiring a continuous energy supply, showing 8 compression steps ranging between 50 and 54 nm. The feasibility we demonstrated of mechanically fine-tuning the compression distance might prove to be a valuable addition to the previously demonstrated electrostatic tuning. To better understand the practical implications of our mechanism, future research could focus on the real-world behaviour when implementing it into a MEMS accelerometer to compensate the TDB. We invite the scientific community to build upon these findings, addressing the identified discrepancies and exploring the broader implications of our work.

REFERENCES

[1] H.-F. Liu, Z.-C. Luo, Z.-K. Hu, S.-Q. Yang, L.-C. Tu, Z.-B. Zhou, and M. Kraft, “A review of high-performance mems sensors for resource exploration and geophysical applications,” *Petroleum Science*, vol. 19, no. 6, pp. 2631–2648, 2022.

[2] B. A. Boom, A. Bertolini, E. Hennes, R. A. Brookhuis, R. J. Wiegerink, J. Van den Brand, M. Beker, A. Oner, and D. Van Wees, “Nano-g accelerometer using geometric anti-springs,” in *2017 IEEE 30th International Conference on Micro Electro Mechanical Systems (MEMS)*. IEEE, 2017, pp. 33–36.

[3] R. Middlemiss, A. Samarelli, D. Paul, J. Hough, S. Rowan, and G. Hammond, “Measurement of the earth tides with a mems gravimeter,” *Nature*, vol. 531, no. 7596, pp. 614–617, 2016.

[4] B. El Mansouri, L. M. Middelburg, R. H. Poelma, G. Q. Zhang, H. W. van Zeijl, J. Wei, H. Jiang, J. G. Vogel, and W. D. van Driel, “High-resolution mems inertial sensor combining large-displacement buckling behaviour with integrated capacitive readout,” *Microsystems & nanoengineering*, vol. 5, no. 1, p. 60, 2019.

[5] A. K. Dokoupil, M. G. Beker, T.-J. Peters, H. L. M. Heeres, and A. Bertolini, “Towards nano-g sensing for high precision orbital manoeuvres,” *Papers of ESA GNC-ICATT 31*, 2023.

[6] G. Dai, M. Li, X. He, L. Du, B. Shao, and W. Su, “Thermal drift analysis using a multiphysics model of bulk silicon mems capacitive accelerometer,” *Sensors and Actuators A: Physical*, vol. 172, no. 2, pp. 369–378, 2011.

[7] J. He, J. Xie, X. He, L. Du, and W. Zhou, “Analytical study and compensation for temperature drifts of a bulk silicon mems capacitive accelerometer,” *Sensors and Actuators A: Physical*, vol. 239, pp. 174–184, 2016.

[8] H. Zhang, X. Wei, Y. Gao, and E. Cretu, “Analytical study and thermal compensation for capacitive mems accelerometer with anti-spring structure,” *Journal of Microelectromechanical Systems*, vol. 29, no. 5, pp. 1389–1400, 2020.

[9] B. Boom, “Acceleration sensing at the nano-g level development and characterisation of low-noise microseismometers for next generation gravitational wave detectors,” 2020.

[10] C. Bourgeois, E. Steinsland, N. Blanc, and N. De Rooij, “Design of resonators for the determination of the temperature coefficients of elastic constants of monocrystalline silicon,” in *Proceedings of International Frequency Control Symposium*. IEEE, 1997, pp. 791–799.

[11] M. A. Hopcroft, W. D. Nix, and T. W. Kenny, “What is the young’s modulus of silicon?” *Journal of microelectromechanical systems*, vol. 19, no. 2, pp. 229–238, 2010.

[12] E. J. Ng, V. A. Hong, Y. Yang, C. H. Ahn, C. L. Everhart, and T. W. Kenny, “Temperature dependence of the elastic constants of doped silicon,” *Journal of microelectromechanical systems*, vol. 24, no. 3, pp. 730–741, 2014.

[13] Y. Okada and Y. Tokumaru, “Precise determination of lattice parameter and thermal expansion coefficient of silicon between 300 and 1500 k,” *Journal of applied physics*, vol. 56, no. 2, pp. 314–320, 1984.

[14] F. W. DelRio, R. F. Cook, and B. L. Boyce, “Fracture strength of micro- and nano-scale silicon components,” *Applied Physics Reviews*, vol. 2, no. 2, 2015.

[15] L. L. Howell, A. Midha, and T. W. Norton, “Evaluation of equivalent spring stiffness for use in a pseudo-rigid-body model of large-deflection compliant mechanisms,” 1996.

[16] L. L. Howell, S. P. Magleby, and B. M. Olsen, *Handbook of compliant mechanisms*. John Wiley & Sons, 2013.

[17] L. L. Howell and A. Midha, “A loop-closure theory for the analysis and synthesis of compliant mechanisms,” 1996.

[18] J. Wu, S. Wang, and J. Miao, “A mems device for studying the friction behavior of micromachined sidewall surfaces,” *Journal of Microelectromechanical Systems*, vol. 17, no. 4, pp. 921–933, 2008.

[19] E. T. Enikov, S. S. Kedar, and K. V. Lazarov, “Analytical model for analysis and design of v-shaped thermal microactuators,” *Journal of Microelectromechanical Systems*, vol. 14, no. 4, pp. 788–798, 2005.

[20] Y. Ohishi, J. Xie, Y. Miyazaki, Y. Aikebaier, H. Muta, K. Kurosaki, S. Yamanaka, N. Uchida, and T. Tada, “Thermoelectric properties of heavily boron-and phosphorus-doped silicon,” *Japanese journal of applied physics*, vol. 54, no. 7, p. 071301, 2015.

[21] G. Masetti, M. Severi, and S. Solmi, “Modeling of carrier mobility against carrier concentration in arsenic-, phosphorus-, and boron-doped silicon,” *IEEE Transactions on electron devices*, vol. 30, no. 7, pp. 764–769, 1983.

[22] C. J. Glassbrenner and G. A. Slack, “Thermal conductivity of silicon and germanium from 3 k to the melting point,” *Physical review*, vol. 134, no. 4A, p. A1058, 1964.

[23] N. Ono, K. Kitamura, K. Nakajima, and Y. Shimanuki, “Measurement of young’s modulus of silicon single crystal at high temperature and its dependency on boron concentration using the flexural vibration method,” *Japanese Journal of Applied Physics*, vol. 39, no. 2R, p. 368, 2000.

[24] Y. Zhu, A. Corigliano, and H. D. Espinosa, “A thermal actuator for nanoscale in situ microscopy testing: design and characterization,” *Journal of micromechanics and microengineering*, vol. 16, no. 2, p. 242, 2006.

[25] D. Brown, W. Christian, and R. M. Hanson, “Tracker: Video analysis and modeling tool,” retrieved January 29, 2024, from https://physlets.org/tracker/.

[26] “Overview of materials for acrylic, cast,” 2024, retrieved February 22, 2024, from https://www.matweb.com/search/DataSheet.aspx?MatGUID=a5e93a1f1fff43bcbac5b6ca51b8981f.

[27] S. Bouissou, J. Petit, and M. Barquins, “Normal load, slip rate and roughness influence on the polymethylmethacrylate dynamics of sliding 1. stable sliding to stick-slip transition,” *Wear*, vol. 214, no. 2, pp. 156–164, 1998.

[28] B. Bhushan and X. Li, “Micromechanical and tribological characterization of doped single-crystal silicon and polysilicon films for microelectromechanical systems devices,” *Journal of Materials Research*, vol. 12, pp. 54–63, 1997.

[29] R. R. Reddy, Y. Okamoto, and Y. Mita, “An on-chip micromachined test structure to study the tribological behavior of deep-rie mems sidewall surfaces,” *IEEE Transactions on Semiconductor Manufacturing*, vol. 33, no. 2, pp. 187–195, 2020.

[30] T. E. Buchheit and L. M. Phinney, “Fracture strength characterization for 25 micron and 125 micron thick soi-mems structures,” *Journal of Micromechanics and Microengineering*, vol. 25, no. 7, p. 075018, 2015.